

Evaluating radiation impact on transmon qubits in above and underground facilities

Francesco De Dominicis,^{1,2,*} Tanay Roy ^{*,3,†} Ambra Mariani,^{4,‡} Mustafa Bal,³ Nicola Casali,⁴ Ivan Colantoni,^{5,4} Francesco Crisa,⁶ Angelo Cruciani,⁴ Fernando Ferroni,^{1,4} Dounia L Helis,² Lorenzo Pagnanini,^{1,2} Valerio Pettinacci,⁴ Roman Pilipenko,³ Stefano Pirro,² Andrei Puiu,² Alexander Romanenko,³ Marco Vignati,^{4,7} David v Zanten,³ Shaojiang Zhu,³ Anna Grassellino,³ and Laura Cardani⁴

¹*Gran Sasso Science Institute, L'Aquila I-67100, Italy*

²*INFN – Laboratori Nazionali del Gran Sasso, Assergi (L'Aquila) I-67100, Italy*

³*Superconducting Quantum Materials and Systems Division,*

Fermi National Accelerator Laboratory (FNAL), Batavia, IL 60510, USA

⁴*INFN – Sezione di Roma, Roma I-00185, Italy*

⁵*Consiglio Nazionale delle Ricerche, Istituto di Nanotecnologia*

⁶*Illinois Institute of Technology*

⁷*Dipartimento di Fisica, Sapienza Università di Roma, Roma I-00185, Italy*

(Dated: August 8, 2024)

Superconducting qubits can be sensitive to abrupt energy deposits caused by cosmic rays and ambient radioactivity. Previous studies have focused on understanding possible correlated effects over time and distance due to cosmic rays. In this study, for the first time, we directly compare the response of a transmon qubit measured initially at the Fermilab SQMS above-ground facilities and then at the deep-underground Gran Sasso Laboratory (INFN-LNGS, Italy). We observe the same average qubit lifetime T_1 of roughly 80 microseconds at both above and underground sites despite having very different radiation levels. We then apply a fast decay detection protocol and investigate the time structure, sensitivity and relative rates of triggered events due to radiation versus intrinsic noise, comparing above and underground performance of several high-coherence qubits with similar design. When comparing above and underground results, we do not observe a significant difference in radiation induced-like events for these sapphire and niobium-based transmon qubits. We conclude that the majority of these events are not radiation-related and can be attributed to other noise sources, which predominantly contribute to single qubit errors in modern transmon qubits. Using gamma sources with increasing activity, we assess the response of the qubit to different levels of radiation in an environment with minimal background radiation. Results indicate that qubits respond to gamma sources, demonstrating the possibility to detect particle impacts. However, radiation events can be observed only by significantly reducing other noise sources, which compromises detection efficiency.

In recent decades, superconducting circuits have emerged as a leading technology for applications in the fields of quantum information [1–6], photon, and particle detectors [7–16]. In the past years, several research groups have started investigating the effect of particle interactions on the performance of quantum bits (qubits) [17, 18]. There are many studies examining these potential effects in superconducting quantum devices of various geometries and materials. Some early work indicated that the lifetime of a transmon qubit could potentially decrease when exposed to a strong radioactive source [19]. Moreover, the effect of high energy deposits can rapidly propagate from the initial location of deposition, affecting multiple qubits and potentially leading to a general chip failure [20, 21]. C.D. Wilen et al. [22] observed that the rate of charge jumps experienced by an array of charge-sensitive qubits (operated as electrometers) was consistent with the rate expected from interactions due to ambient radioactivity and cosmic rays.

Thorbeck et al. [23] did not observe significant radiation effects, but concluded that the impacts due to ionizing radiation may induce frequency jumps in a dominant loss mechanism, namely two-level systems (TLSs) [24–31], possibly affecting qubit stability.

Other studies have shown that suppressing radioactivity can enhance the performance of superconducting circuits. Operating the device in a radio-pure facility has allowed for the suppression of correlated errors [32] significantly improving the locking of a fluxonium qubit at the sweet spot [33] and enhancing the internal quality factor of superconducting resonators [34]. The latter publication also determined that the substrate on which qubits are deposited, rather than the qubits themselves, is the primary target for particle interactions.

These findings have motivated efforts in further directions aimed at studying and mitigating possible effects of radioactivity. Promising results have been achieved by equipping the chip with “traps” designed to absorb phonons produced (also) by radioactive interactions [35–37] and using gap engineering [18, 38]. Some groups are also focusing on the components used to construct and operate qubits [39, 40], as it has been demonstrated that some of them, such as the Printed Circuit Boards (PCBs), can produce a sizeable rate of events in the qubit

* Equal contribution

† Corresponding author: roytanay@fnal.gov

‡ Corresponding author: ambra.mariani@roma1.infn.it

chip [41]. Furthermore, it is also worth mentioning recent proposals of equipping qubits with a device specialized in recognizing particle interactions [42] or with external muon detectors [21, 38, 43].

In this work, for the first time, we study charge-insensitive transmon qubit devices in two laboratories with very distinct radiation environments, as part of the Superconducting Quantum Materials and Systems (SQMS) Center *Round Robin* project [41], which aims to study identical qubits measured at multiple test sites around the world. We first compare the average relaxation time of a qubit measured over several hours both above ground at Fermilab and deep underground at Gran Sasso Laboratory. We then employ a fast decay detection protocol to investigate radiation-induced events in similar transmon qubits and analyze the time structure, sensitivity, and relative rates of triggered events due to radiation versus intrinsic noise. To further study the qubit's response to radiation, we expose the superconducting chip to gamma-ray sources with increasing activity in a controlled environment with minimal background radiation and estimate timescales at which radiation may become concerning for quantum computational errors.

I. EXPERIMENTAL LOCATIONS

To perform the comparative study, we operated similar transmon chips (charge-insensitive) in two different laboratories: the *Quantum Garage* of the SQMS Center at Fermilab (FNAL, Illinois, US), and the *Ieti Facility* located in the deep-underground Gran Sasso Laboratory of INFN (INFN-LNGS, L'Aquila, Italy). The chip consisted of a $432\ \mu\text{m}$ thick, $7.5\times 7.5\ \text{mm}^2$ wide HEMEX grade Sapphire substrate. It is noteworthy that the entire substrate is covered in Niobium creating a ground plane; this may act as a phonon trap, diminishing the phonon propagation and absorption in the active part of the qubit [44, 45]. Eight Niobium transmons with different geometries were deposited on the chip (see Supplementary section A); their surface was capped using a $\sim 10\ \text{nm}$ thick layer of Gold (measured at both sites) or Tantalum (measured at FNAL) to reduce losses due to the formation of Nb_2O_5 [46]. The capping technique allowed us to achieve excellent T_1 of many tens and up to hundreds of microseconds, which is crucial for studying changes in a qubit's lifetime at microsecond timescales. We characterized several qubits of these chips operated at FNAL and at INFN-LNGS, and performed comparisons for either an identical qubit (standard T_1 experiment only) or qubits of similar geometries and materials.

To predict the rate of impacts due to ambient radiation, we conducted a Monte Carlo simulation using the GEANT4 framework [47] developed in Ref. [41]. We anticipate the total rate of radiation events interacting within the chip at FNAL and INFN-LNGS to be $(57\pm 3)\times 10^{-3}$ events/sec and $(4.0\pm 0.6)\times 10^{-3}$ events/sec, respectively. Table I provides a summary of the simula-

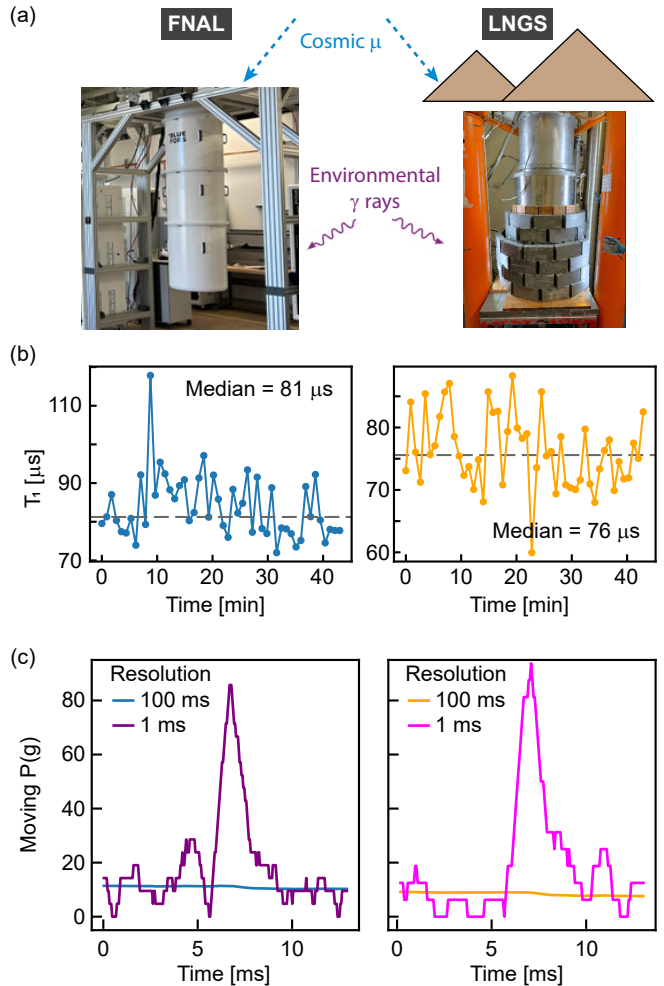


FIG. 1. **Comparison of the two experimental sites.** (a) The above-ground cryostat at FNAL is not protected from any radiation, whereas, the deep-underground one at LNGS is strongly guarded from cosmic muons by the 1.4 km deep rock overburden and from environmental γ rays through a copper plus lead shield. The left and right panels present data taken at FNAL and LNGS, respectively. (b) Standard T_1 measurements performed on the same device for a long period show similar fluctuations. These measurements are slow and cannot capture the T_1 drops at millisecond time scales potentially due to radiation impact. (c) The graphs display the moving probability of detecting the qubit in $|g\rangle$ with 1 ms and 100 ms time resolution (see Fig. 2(c)). The features (purple and pink traces) corresponding to low T_1 periods obtained with 1 ms resolution at two laboratory locations show very similar profile. The low resolution traces (blue and orange) clearly show that an event will go undetected and thus cannot be observed with regular T_1 experiments due to its averaging nature.

tion results, with detailed information provided in the Supplementary Section B.

At FNAL (see Fig. 1(a), left panel), the rate is primarily dominated by γ rays produced by the decay of naturally radioactive isotopes present in the laboratory environment. However, muons generated by cosmic rays

Source	FNAL [events/sec]	INFN-LNGS [events/sec]
Lab γ -rays	$(46 \pm 2) \times 10^{-3}$	$(1.3 \pm 0.1) \times 10^{-3}$
Muons	$(8 \pm 0.5) \times 10^{-3}$	$< 10^{-5}$
Setup	$(2.7 \pm 0.5) \times 10^{-3}$	$(2.7 \pm 0.5) \times 10^{-3}$
Total	$(57 \pm 3) \times 10^{-3}$	$(4.0 \pm 0.6) \times 10^{-3}$

TABLE I. **Simulated rate of interactions in the Sapphire substrate.** For the computation of the FNAL rates, we assumed a “standard” γ -ray flux of $(2.5 \pm 0.5) \gamma/\text{cm}^2/\text{sec}$ and a muon flux of $1 \mu/\text{cm}^2/\text{min}$. For INFN-LNGS, we measured a flux in the experimental room of $(1.0 \pm 0.5) \gamma/\text{cm}^2/\text{sec}$; the suppression factor due to the lead and copper shields surrounding the chip was evaluated through a Monte Carlo simulation. Finally, the radioactive contamination of the components of the setup was measured in Ref. [41].

also contribute significantly to the overall rate. In contrast, at INFN-LNGS (see Fig. 1(a), right panel), muons are suppressed by six orders of magnitude thanks to the 1.4 km thick rock overburden. Moreover, the radioactivity of the laboratory is substantially reduced by copper and lead shields positioned both inside and around the refrigerator. The last source of radioactivity arises from the materials constituting the qubit chip and its nearby read-out components. In a previous study conducted within the SQMS *Round Robin* project [41], we measured the radioactive content of each component and determined that cables, connectors, amplifiers, circulators, etc., have a negligible impact on the total event rate. The only exception is the PCB, which is typically highly contaminated and located in close proximity to the chip. In this setup, the PCBs are responsible for the whole counting rate reported in the line “Setup” of Table I. While this rate is negligible at FNAL, it becomes the dominant source of radioactivity at INFN-LNGS, where all external sources of radioactivity are suppressed.

Furthermore, at INFN-LNGS, we utilize calibrated Thorium radioactive sources to increase the event rate up to one event every two seconds and investigate the chip behaviour in a “high”-radiation environment.

II. EFFECT OF RADIATION IMPACT

When a particle impinges on the qubit chip, it releases energy. Muons create long tracks across the chip, whereas γ rays interact through photo-electric absorption or (mainly via) Compton scattering, producing short-track electrons. In the absence of an electric field, the thousands of charges created along the ionizing track recombine into phonons, which diffuse throughout the chip [22]. As illustrated in Fig. 2(a), when phonons interact with a superconductor, they can break Cooper pairs into quasiparticles. Subsequently, when one or more quasiparticles tunnel through the Josephson Junction, the qubit loses its energy and quickly decays to its ground state $|g\rangle$ [36] with a timescale of 0.16-1.6

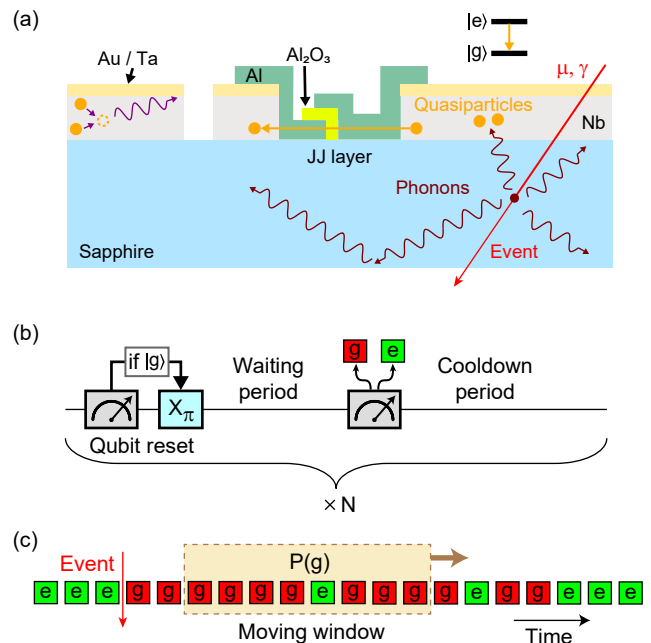


FIG. 2. **Quasiparticle generation process and experimental protocol.** (a) Sketch of the quasiparticles generation process due to particle interactions in the substrate. Ionizing radiation impinging on the substrate produces electron-hole pairs, which recombine creating phonons. These phonons spread throughout the chip and, in superconducting structures, can break Cooper pairs into quasiparticles, which can tunnel across the Josephson Junction inducing decay of the qubit from the excited state $|e\rangle$ to the ground state $|g\rangle$. (b) The fast decay detection protocol consists of repeated cycles of preparation in the excited state, waiting period, measurement and cooldown periods. The duration of each cycle is less than $90 \mu\text{s}$, while the waiting time is 5 or $10 \mu\text{s}$. (c) During normal periods, the qubit is highly likely to be found in the excited state due to its long T_1 . An event, such as ionizing radiation, causes a drastic reduction in qubit’s lifetime, resulting in repeated detections in $|g\rangle$ and thus increasing the probability $P(g)$ of finding the qubit in $|g\rangle$ within a suitably chosen time window. Over time, the qubit gradually recovers its natural T_1 . The measured sequence is then analyzed to detect radiation impacts with sub-millisecond resolution.

μs [48, 49]. Since the metallic pads of the transmon host a large number of quasiparticles that take some time to dissipate through normal metal (PCB leads) or lower-energy phonon scattering, these tunneling events can continue to occur, causing the qubit to suffer from strong relaxation for some time. Previous studies claim this low T_1 periods last from one to several tens of milliseconds [20, 21]. We investigated these type of events in our studies.

We first performed standard T_1 experiments on both underground and above-ground locations on the identical qubit Q1 and monitored the relaxation times for close to an hour. These experiments were slow, and each data point took about 50 seconds to complete. The results, plotted in Fig. 1(b), show similar mean values and fluc-

tuations, typical for transmon qubits [46], demonstrating that radiation has no significant effect at current standard transmon qubit lifetimes of ~ 100 microseconds. No sudden drop in T_1 values was observed. This was expected as the standard T_1 experiments, due to their averaging nature, are not sensitive to fluctuations at millisecond timescales. In order to study possible events at such a time resolution we employed a protocol, tailored for single qubits, utilizing fast decay measurements [18, 20].

The fast detection protocol illustrated in Fig. 2(b) begins by resetting the qubit in its excited state $|e\rangle$. This is accomplished by initially measuring the qubit and applying a conditional π -pulse if the qubit is found to be in the state $|g\rangle$ via fast feedback. Following a waiting period Δt_d lasting a few microseconds, the qubit is measured again to determine whether it is in state $|g\rangle$ or $|e\rangle$. Given a sufficiently long qubit T_1 , the qubit is highly likely to be found in state $|e\rangle$. Theoretically, the qubit relaxes to state $|g\rangle$ only a small fraction of the time, given by $(1 - e^{-\Delta t_d/T_1}) \approx \Delta t_d/T_1$. However, a radiation event significantly reduces T_1 , making it highly probable for the qubit to be detected in state $|g\rangle$. The sequence is then repeated after another short period, allowing the chip to cool down. Since the effect of quasiparticle generation persists longer than the time taken for one sequence, an event due to radiation typically results in repeated detection in state $|g\rangle$, as depicted in Fig. 2(c).

In our measurements, we select a fixed waiting period of 5 or 10 μs ; the readout pulse has a length ranging from 3.8 to 8 μs (the individual parameters of each measurement are reported in Table S1 of the Supplementary Section A). The π -pulse has a negligible length ($< 1 \mu\text{s}$). The cool-down period (10 to 70 μs) is chosen to ensure that the transmon does not exhibit excessive population in the second excited state $|f\rangle$. Nevertheless, a simultaneous fit of the $|g\rangle$, $|e\rangle$ and the second excited state $|f\rangle$ showed that there were many moments in which the $|f\rangle$ (and sometimes even the third excited state $|h\rangle$) states were populated. To ensure data consistency, we exclude these time intervals. A thorough investigation of this phenomenon will be mandatory for applications in sensing, as this selection significantly limits the measurement's live-time (see Table II).

The readout scheme employed is detailed in the Supplementary Section C. The input signal, filtered through attenuators, low-pass filters, and infrared filters, is sent to the qubit; the output signal is fed into cryogenic triple-junction isolators, and then amplified via a cryogenic HEMT followed by a room temperature amplifier. The qubit readout and control are performed through an RF-SoC board using the Quantum Instrumentation Control Kit (QICK) [50]. Each measurement generates a complex number (I/Q values) that are post-processed to distinguish between $|g\rangle$ and $|e\rangle$ based on readout calibration.

We acquired the data for several hours containing several hundred million readouts. During the initial analysis, we simply computed the probability $P(g)$ of finding a qubit in $|g\rangle$ for a fixed time window and plotted $P(g)$ as

Datasets	acquisition time	live-time
	[min]	[min]
Shielded chip	736.7	28.2
44 kBq Th Source	620.7	114.0
76 kBq Th Source	124.1	46.3
125 kBq Th Source	62.1	23.7
161 kBq Th Source	62.1	62.1
FNAL Q2	234.6	104.1
FNAL Q3	449.7	92.8
FNAL Q4	243.1	25.9

TABLE II. **List of datasets.** Top rows correspond to data taken at LNGS using Q1. The original duration (acquisition time) and ‘live-time’ duration after removing period of time where the second excited state $|f\rangle$ is highly populated are shown. Datasets taken at FNAL correspond to measurements on three different qubits on the same chip.

we moved the window (see Fig. 2(c)). A typical record of $P(g)$ as a function of time is shown in Fig. 3(a). The magenta color is the mean of the trace while the fluctuations in the trace look steady. A clear spike around 18.2 seconds corresponds to an event with drastic T_1 drop. When zoomed in, these spikes show different pulse shapes as plotted in Fig. 3(b). These pulses generally have a sharp rise, but the fall times vary between different instances. As depicted in Fig. 1(b), we found pulses of similar time-profile at both locations irrespective of the specific qubit, indicating that the drop in relaxation time is not tied to a specific transmon. All pulses observed in our studies last less than ten milliseconds in agreement with the study in Ref. 21, and thus these pulses require multiple qubit measurements within a millisecond for being detected. For example, the pulses in Fig. 1(c) are visible when a one ms time-window is selected for computing $P(g)$ and the signal vanishes when a coarse time-window of 100 ms is chosen. Clearly, a slow measurement scheme will not be able to resolve individual radiation impact events. In other words, standard T_1 measurements, due to their slow nature, will not be affected by radiation impacts (happening at intervals of several seconds).

A simple detection strategy based on triggering pulses on the $P(g)$ data by setting a constant threshold, however, suffers from the problem that a large threshold misses many events, whereas, a lower value picks up a lot of noise arising inherently from the qubit measurement. Furthermore, such a noise is not stable in time leading to unexpected variations in the rate. As shown in Fig. 3(c), the $P(g)$ traces occasionally show noisy behavior which do not follow any adjacent spike. These periods of instability can last from sub-seconds to a minute and will affect regular T_1 experiments. Even though it appears to be related to TLS scrambling, we currently do not have a clear understanding of the source of this behavior, and it will be a subject of future studies. To better identify radiation-induced events, we developed a modified strategy discussed below.

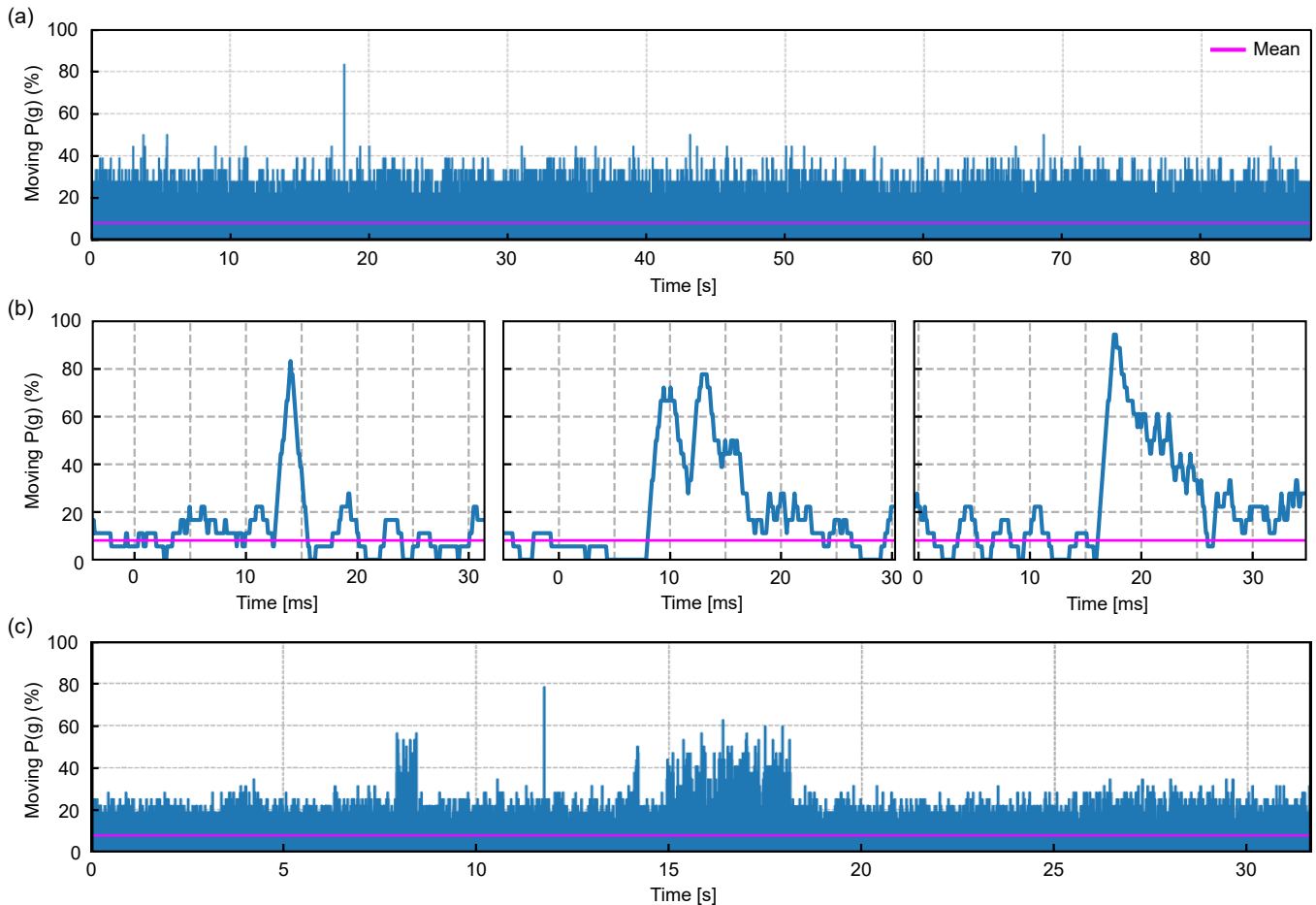


FIG. 3. **Typical signal traces and occasional instability.** (a) An 88 second long trace showing a single spike corresponding to a drastic drop in T_1 . (b) Three different pulse shapes are shown. All these pulses start with a fast rise. (c) The qubits sporadically undergo periods of instability lasting for up to a minute visible in a small fraction of data acquired.

III. EVENT SELECTION

Several considerations are applied to the analysis for the selection of events. Initially, we perform a simultaneous 2D Gaussian fit to the distribution of I/Q values for the states $|g\rangle$, $|e\rangle$, and $|f\rangle$. To correct for time instabilities, we remove traces where the qubit is found in the second excited state $|f\rangle$. The clouds corresponding to $|g\rangle$ and $|e\rangle$ are then rotated to align along one quadrature and projected onto the other. Further information can be found in the Supplementary Section D.

Once the I/Q clouds are projected onto one quadrature, a threshold is chosen in order to convert the measured I/Q values into a sequence of 0s (for $|g\rangle$) and 1s (for $|e\rangle$). Since the two clouds are not completely separated, every value of the threshold will lead to some errors in the state identification. In our analysis, we calculate the fraction of measurements for each state falling on the wrong side of the threshold (misidentification) and choose the threshold value that minimizes the sum of these two fractions (total error). This is done by fitting the clouds with 1D Gaussian functions and integrating the tails falling on

the wrong side of the threshold, varying the candidate threshold value until the minimum is found. The resulting threshold values allow for the correct identification of the qubit state in 90% to 95% of measurements, with fluctuations of a few percentage points depending on the specific qubit and dataset considered.

The sequence of 0s and 1s is then organized into traces of 10^6 points. We expect that radiation-induced events last at least one millisecond, which, given the sampling periods reported in Table III, corresponds to approximately 12–35 zeros. According to the same table, we anticipate a baseline of 8–15% of zeros arising from spontaneous qubit decay. Therefore, we require the detection of at least four consecutive zeros to trigger an event. This criterion ensures reasonable signal efficiency while significantly reducing false triggers caused by qubit spontaneous decay and other types of noise. Indeed, the number of times we measure the qubit in state $|g\rangle$ can be due to different phenomena, which can be summarized as follows:

1. Qubit spontaneous decay: The probability of finding the qubit in state $|g\rangle$ can be roughly estimated

by $1 - e^{-\Delta t_d/T'_1}$, where T'_1 is an “effective” relaxation time computed using 10^6 points (corresponding to approximately one minute of data) to monitor changes over time, and Δt_d is the waiting period (see Table III) between the state preparation in $|e\rangle$ and end of readout. We then use the average of the T'_1 values obtained from each data segment to estimate the probability of the qubit being in state $|g\rangle$ for each dataset. Further details can be found in Supplementary Section E.

2. Ionizing radiation: We use Geant4-based Monte Carlo simulations to predict the number of impacts on the qubit chip.
3. Other sources of noise: These involve electronic noise, luminescence or relaxation of materials at low temperature [51] (known sources of quasiparticle poisoning include the holder or the interface between the holder and the chip [52–54] and relaxations of metal films [53, 55]), vibrations [56], etc.

Once the trigger is fired, we acquire a 160-point window divided as follows:

- A 60-point long ($[0, 59]$) pre-trigger region to estimate the average number of zeros (noise) before the events;
- A 40-point long ($[60, 99]$) dead region to avoid signal leakage into the pre-trigger region;
- A 60-point long ($[100, 159]$) signal region. Specifically, we acquire 10 points before the trigger and 50 after the trigger.

Datasets	Δt_d [μ s]	$\langle T'_1 \rangle$ [μ s]	$P(g)$ [%]	T_S [μ s]	$r_{\text{decay}}^{4\text{zeros}}$ [events/sec]
Shielded chip	14	118.6	11.1	73.7	2.3 ± 0.4
44 kBq Source	11	76.3	13.4	67.7	5.4 ± 1.1
76 kBq Source	11	79.9	12.9	67.7	4.6 ± 0.9
125 kBq Source	11	68.9	14.8	67.7	7.2 ± 1.5
161 kBq Source	11	74.1	13.8	67.7	6.1 ± 1.2
FNAL Q2	14	162.7	8.2	88.0	0.5 ± 0.1
FNAL Q3	9	63.8	13.2	84.3	4.1 ± 0.8
FNAL Q4	13	165.5	7.6	31.7	1.1 ± 0.2

TABLE III. **Datasets parameters.** Relevant parameters for each dataset. Δt_d is the sum of the waiting and readout times, $\langle T'_1 \rangle$ is the average relaxation time, $P(g) = 1 - e^{-\Delta t_d/T'_1}$ is the expected ground state probability, T_S is the sampling period and $r_{\text{decay}}^{4\text{zeros}}$ is the rate of events in which we expect the qubit spontaneous decay to result in four consecutive zeros (and thus, in a triggered event). The top rows refer to datasets acquired at LNGS using Q1 (in the fully shielded configuration and using Th sources), while the bottom rows refer to data taken at FNAL using three different qubits on the same chip.

The choice of the window length was based on the signal features. Given a sampling period of 0.03–0.09 milliseconds, and considering that an event lasts a few milliseconds (see Fig. 1), we expect the event to be fully contained within a 60-point window. To prevent re-triggering, we apply a dead-time of 51 points after the trigger.

As shown in Table III, we expect from 0.5 up to 7 events per second due to qubit spontaneous decay alone, depending on the dataset. These rates are about one to two orders of magnitude higher than those expected from ambient radiation (0.004 and 0.057 events/sec at LNGS and FNAL, respectively) or gamma ray sources (0.12 to 0.43 events/sec).

To identify events caused by ionizing radiation, we employ a systematic approach aimed at minimizing contributions from qubit spontaneous decay. For each dataset, we compute the probability of observing more than a certain number of zeros in a sequence of 60 measurements, corresponding to the length of the signal window. This probability is derived from the cumulative distribution function (CDF) of the Binomial distribution calculated over 60 points. Based on these probabilities, we set thresholds on the minimum number of zeros required within the signal region to significantly reduce the expected rate of qubit spontaneous decay, targeting values approximately an order of magnitude lower than those expected from ionizing radiation.

Additionally, we establish thresholds on the maximum number of zeros allowed in the pre-trigger region. In this region, the number of zeros should be consistent with those predicted by the qubit decay. A significantly larger number of zeros would indicate transient noise that could induce false triggers and has to be discarded from the analysis. Therefore, we calculate the Binomial probability of observing a specific number of zeros in the pre-trigger region and apply a cut for probabilities below 1%. Detailed thresholds used for each dataset are provided in Supplementary Section F.

IV. RESULTS AND DISCUSSION

The distributions of the number of zeros in the signal region for the triggered events are depicted in Fig. 4. These distributions correspond to background runs conducted at the fully shielded facility at LNGS without any Thorium source and at FNAL, where qubits were entirely exposed to cosmic rays and gamma radiation in the laboratory environment. It can be observed that the histograms of Q1 and Q3, which have similar $P(g)$ values, also exhibit similar shapes. This observation holds true for Q2 and Q4 as well.

As described in the previous section, to identify radiation-induced events, we reduce qubit spontaneous decay events to negligible rates by setting a threshold on the minimum number of zeros in the signal region. For example, for the LNGS–Q1 and FNAL–Q3 datasets,

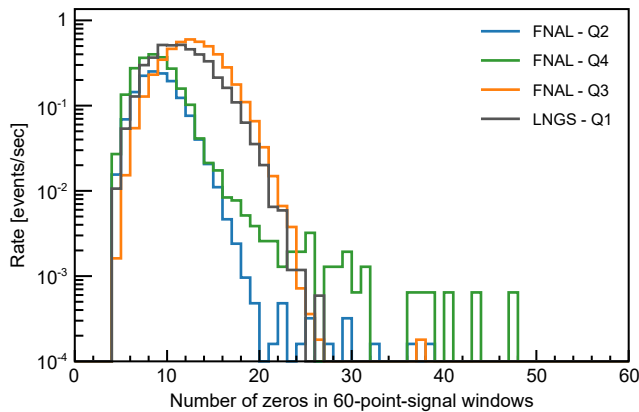


FIG. 4. **Distribution of zeros in the signal region for background runs conducted at the deep-underground LNGS and the above-ground FNAL.** At FNAL the qubits were completely unshielded from cosmic and ambient gamma radiation. The majority of events is due to qubit spontaneous decay. The histograms of Q1 and Q3, which share similar $P(g)$ values, display comparable shapes. This similarity is also evident between Q2 and Q4.

which feature a similar $P(g)$, we required at least 23 zeros (non-consecutive) in order to have a negligible rate from qubit spontaneous decay. In contrast, for FNAL-Q2 and FNAL-Q4, we required at least 18 zeros due to the lower $P(g)$. We emphasize that such a stringent requirement discards the vast majority of the events (see Fig. 4).

Additionally, a maximum number of zeros in the pre-trigger region is set to mitigate noisy periods. This number ranges from a minimum of 10, for datasets with lower $P(g)$ to a maximum of 15 for datasets with higher $P(g)$. The cuts on the number of zeros in the pre-trigger and in the signal regions for all the datasets are reported in Table S4 of the Supplement. Table IV summarizes the results obtained from the background runs conducted at LNGS and FNAL. The three qubits operated on the same chip at FNAL show rates ranging from 3 to 25×10^{-3} events/sec, in contrast to what we would expect if the selected events were dominated by radioactivity. In this case, indeed, the rates should have been similar. Moreover, the rate measured in the fully shielded facility at LNGS is comparable with the one measured at FNAL. If the obtained values were ascribed to radioactivity, the LNGS rate should have been an order of magnitude smaller than the FNAL one. These results suggest that modern transmons are primarily affected by sources of noise other than radiation, contributing significantly to the reduction in T_1 at short timescales. This fact has also been corroborated by another recent study [38], where cosmic rays were not identified as a major contributor to the most frequent correlated errors (among four qubits).

Finally, we observe that the measured rates are lower than those expected from simulations of ambient radiation. This discrepancy suggests that the event selection substantially reduces the efficiency of radiation-induced

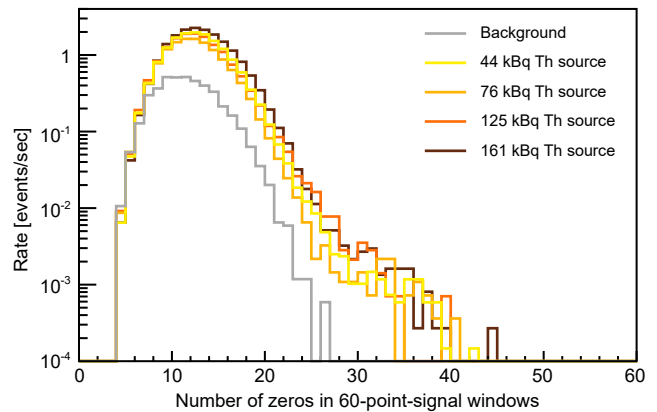


FIG. 5. **Distribution of zeros in the signal region for runs with controlled radioactive sources at deep-underground LNGS.** Data were acquired by exposing the chip to Thorium radioactive sources with increasing activity. For comparison, the distribution for the ‘background’ run without sources is also shown (light grey).

events.

To better investigate the detection efficiency for radiation-induced events, at LNGS, we exposed the chip to Thorium radioactive sources with increasing activity levels. Several commercially available Thorium rods with known activity were inserted inside the copper shield and outside the outer vacuum chamber of the fridge for this study. Data were analyzed using the same protocol used for background runs and reported in Fig. 5. It demonstrates that exposing the chip to a controlled radioactive source results in an excess of events with high number of zeros in the signal region compared to the “shielded” configuration. The rate of these events increases linearly with the intensity of the source itself as visible in Fig. 6.

Next, we compare the triggered and simulated rates for the various Thorium sources. The slope parameter p_1 of the linear fit in Fig. 6 shows that the aggressive data selection leads to a detection efficiency of $(8 \pm 2)\%$, where the uncertainty is statistic only. The systematic uncertainty is much larger, as the signal efficiency depends on the cuts used for data selection, that

Datasets	Measured Rate [events/sec]	Radioactivity Contribution [events/sec]
Shielded chip	$(2.9 \pm 1.3) \times 10^{-3}$	$(4.0 \pm 0.6) \times 10^{-3}$
FNAL Q2	$(3.2 \pm 0.7) \times 10^{-3}$	
FNAL Q3	$(4.7 \pm 0.9) \times 10^{-3}$	$(57 \pm 3) \times 10^{-3}$
FNAL Q4	$(25 \pm 4) \times 10^{-3}$	

TABLE IV. **Results from background runs conducted at LNGS and FNAL on qubits with similar designs.** This Table shows the rates of events selected after applying cuts to minimize qubit spontaneous decay and mitigate noise. The column “Radioactivity Contribution” reports the radiation-induced rates at the two experimental sites predicted through Monte Carlo simulations (see Table I).

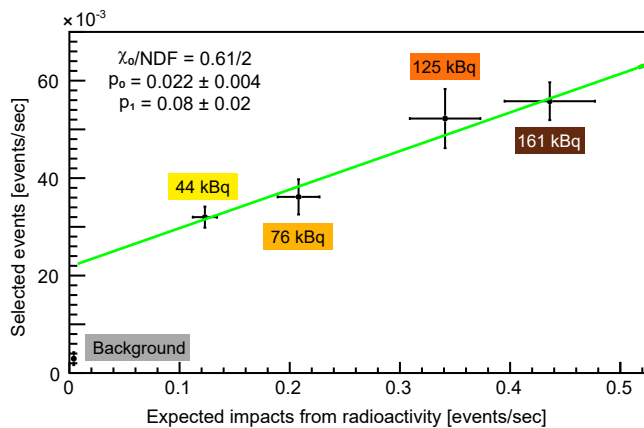


FIG. 6. Measured rate of events for LNGS-Q1 as a function of the rate expected from the simulation. Data were modelled using a first-degree polynomial. The linear coefficient p_1 can be considered as the detection efficiency. The fit was done excluding the background data point measured in the “shielded” configuration. Uncertainties on the triggered rates are statistical only, while uncertainties on the expected impacts are dominated by the systematic uncertainties in the simulation.

vary across the datasets because of the differing T_1 and noise conditions. Therefore, this result should be considered qualitative. Correcting the predicted rate at LNGS (4×10^{-3} event/sec) by this efficiency results in an expected rate from radioactivity of 0.32×10^{-3} event/sec, an order of magnitude smaller than the measured one. This further supports the hypothesis that the measured rates are not dominated by radiation-induced events.

Despite the low detection efficiency, our findings indicate that qubits are sensitive to laboratory gamma radioactivity, even though gamma rays deposit less energy compared to cosmic rays [22, 34]. While the primary objective of this work was not to operate a qubit as a particle detector, it is evident that optimizing the thresholds or trigger algorithms, along with employing more refined pulse reconstruction techniques (such as matched filter algorithms), could significantly improve detection efficiency.

Although we did not experimentally observe a measurable effect of environmental radiation-induced errors, we can utilize the simulated rates to provide an upper estimate for the relevant timescales at which radiation would start to affect quantum computation through information loss occurring on individual qubits. The probability to have at least one event in a time window ΔT is given by $P_{\text{impact}} = 1 - e^{-r \cdot \Delta T}$, where r is the rate of impacts. Using the simulated rates, for environmental radioactivity we find that in a non-shielded laboratory setting a quantum computation would be affected by radioactivity less than 0.1% (1%) times if the computation is completed within approx 17 ms (170 ms). Note that the computation may include multiple runs of an algorithm and not necessarily require to be a single run lasting for ΔT . At a fully shielded environment like LNGS, due to a much

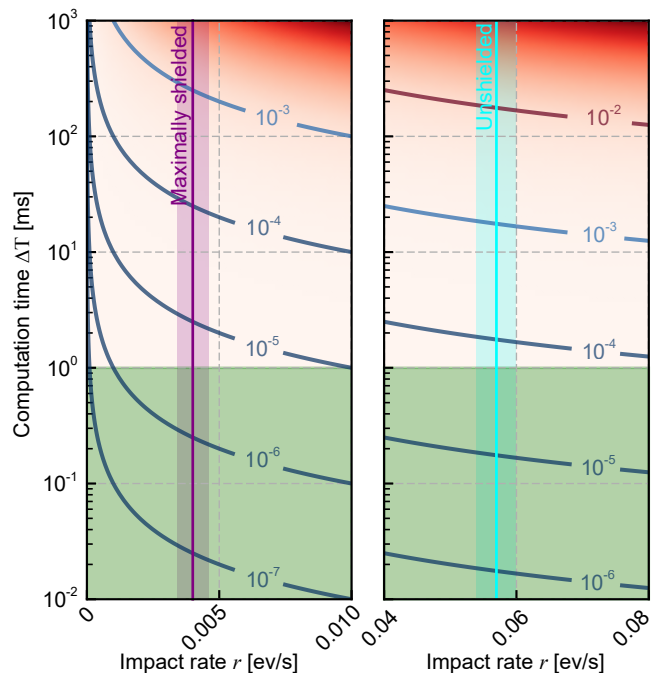


FIG. 7. Relationship between available computational time and radiation rate for different error probability tolerance. The contours show fixed error probability lines as a function of available computational time ΔT and the rate of impacts r . The purple (cyan) vertical line with shaded area show the simulated rate for maximally shielded (LNGS) versus non-shielded. The horizontal green area ($\Delta T < 1$ ms) highlight the lifetimes of modern transmon qubits. The error rates in this regime is less than 10^{-4} making radiation an insignificant contributor.

lower expected rate, we have instead $P_{\text{impact}} < 0.1\%$ (1%) if $\Delta T \lesssim 250$ ms (2.5 s). The available computation period increases if a higher error probability is tolerated. Figure 7 shows available computational time as a function of radiation impact rates around values estimated for the two cases. The contour lines show various constant error rates and the horizontal green shaded area (< 1 ms) represents the T_1 times of contemporary transmon qubits. In this regime, radiation causes error with a minuscule $P_{\text{impact}} < 10^{-4}$. In other words, when a calculation is repeated $> 10^4$ times, one result will be corrupted due to radiation. Most of the modern algorithms running on quantum hardware like variational quantum eigensolver or quantum approximate optimization take less than a millisecond for a single iteration and require a large number of repetitions ($\sim \mathcal{O}(10^4)$). Therefore, we can safely conclude that radiation has a negligible effect on modern transmon-based quantum computing platforms even if error correction fails due to an impact.

V. CONCLUSIONS

We have conducted a comparative study to assess the impact of radiation on transmon qubits at two laboratories with very different radiation environments. Regular T_1 experiments performed on the same qubit show no significant difference in qubit lifetimes of the order of 80 microseconds.

In order to study the time dynamics at short timescales, we employed a fast decay detection protocol utilizing active reset. Multiple similar qubits measured with this technique at Fermilab (above ground and without lead or copper shieldings) showed rates comparable to those from the maximally shielded qubit at the deep-underground Gran Sasso Laboratory. These findings suggest that the radiation-like events observed, which last for milliseconds, originate from different sources, and indicate that radiation is not a major source of errors in modern transmon qubits.

Experiments with controlled Thorium sources at LNGS demonstrate the potential for detecting particle impacts, opening the possibility of using transmons as particle detectors. However, the observed rates are lower than those predicted by simulations, indicating the need for more refined trigger algorithms and/or analysis strategies.

Based on both experimental and simulated results, we estimate that radiation-induced single-qubit errors will affect quantum computation by at most a few percent, with computational times up to 170 ms at fully unshielded facilities and 2.5 s at LNGS.

Future experiments will focus on a more detailed understanding of the various error sources currently overshadowing radiation-induced effects. This will involve further investigations using fast decay detection protocols, exploring different qubit geometries, materials, and synchronized measurements across the same and differ-

ent chips. The SQMS Center aims to enhance the T_1 of transmon qubits, and future studies will examine the performance of qubits with a broad range of coherence times, from tens of microseconds to approaching milliseconds. Advancing this knowledge is crucial for the effective use of superconducting qubits in quantum computation and sensing.

ACKNOWLEDGMENTS

The authors thank the Director and technical staff of the Laboratori Nazionali del Gran Sasso. We are also grateful to the LNGS Computing and Network Service for computing resources and support on U-LITE cluster at LNGS. We thank S. Nisi for the ICP-MS measurements of the PCB, C. Tomei and G. D’Imperio for the maintenance of the simulation software, G. Catelani for the useful discussion. We are grateful to A. Girardi for the controller of the cryogenic switch, M. Guetti for the help with the whole cryogenic facility (including its continuous upgrades), and M. Iannone for the assembly of the device at LNGS. We are thankful to Theodore C. III and Grzegorz Tatkowski for providing support on experimental preparations and cryogenic operations at FNAL.

The work was supported by the U.S. Department of Energy, Office of Science, National Quantum Information Science Research Centers, Superconducting Quantum Materials and Systems (SQMS) Center under the contract No. DE-AC02-07CH11359, by the Italian Ministry of Foreign Affairs and International Cooperation, grant number US23GR09, by the PNRR MUR project CN00000013-ICSC, by the Italian Ministry of Research under the PRIN Contract No. 2020h51338 (“Thin films and radioactivity mitigation to enhance superconducting quantum processors and low temperature particle detectors”) and by the Italian Ministry of Research under the PRIN Contract No. 2022BP4H73 (Chasing Light Dark Matter with Quantum Technologies”).

-
- [1] R. Barends, J. Kelly, A. Megrant, A. Veitia, D. Sank, E. Jeffrey, T. C. White, J. Mutus, A. G. Fowler, B. Campbell, Y. Chen, Z. Chen, B. Chiaro, A. Dunsworth, C. Neill, P. O’Malley, P. Roushan, A. Vainsencher, J. Wenner, A. N. Korotkov, A. N. Cleland, and J. M. Martinis, Superconducting quantum circuits at the surface code threshold for fault tolerance, *Nature* **508**, 500 (2014).
- [2] F. Arute *et al.*, Quantum supremacy using a programmable superconducting processor, *Nature* **574**, 505 (2019).
- [3] M. Kjaergaard, M. E. Schwartz, J. Braumüller, P. Krantz, J. I.-J. Wang, S. Gustavsson, and W. D. Oliver, Superconducting qubits: Current state of play, *Annual Review of Condensed Matter Physics* **11**, 369 (2020).
- [4] Rigetti aspen-m-2 features, <https://www.rigetti.com/what-we-build>.
- [5] Y. Wu, W.-S. Bao, S. Cao, F. Chen, M.-C. Chen, X. Chen, T.-H. Chung, H. Deng, Y. Du, D. Fan, M. Gong, C. Guo, C. Guo, S. Guo, L. Han, L. Hong, H.-L. Huang, Y.-H. Huo, L. Li, N. Li, S. Li, Y. Li, F. Liang, C. Lin, J. Lin, H. Qian, D. Qiao, H. Rong, H. Su, L. Sun, L. Wang, S. Wang, D. Wu, Y. Xu, K. Yan, W. Yang, Y. Yang, Y. Ye, J. Yin, C. Ying, J. Yu, C. Zha, C. Zhang, H. Zhang, K. Zhang, Y. Zhang, H. Zhao, Y. Zhao, L. Zhou, Q. Zhu, C.-Y. Lu, C.-Z. Peng, X. Zhu, and J.-W. Pan, Strong quantum computational advantage using a superconducting quantum processor, *Phys. Rev. Lett.* **127**, 180501 (2021).
- [6] J. Chow *et al.*, Ibm quantum breaks the 100-qubit processor barrier (2021), <https://research.ibm.com/blog/127-qubit-quantum-processor-eagle>.

- [7] A. V. Dixit, S. Chakram, K. He, A. Agrawal, R. K. Naik, D. I. Schuster, and A. Chou, Searching for dark matter with a superconducting qubit, *Phys. Rev. Lett.* **126**, 141302 (2021).
- [8] A. Agrawal, A. V. Dixit, T. Roy, S. Chakram, K. He, R. K. Naik, D. I. Schuster, and A. Chou, Stimulated emission of signal photons from dark matter waves, *Phys. Rev. Lett.* **132**, 140801 (2024).
- [9] P. K. Day, H. G. LeDuc, B. A. Mazin, A. Vayonakis, and J. Zmuidzinas, A broadband superconducting detector suitable for use in large arrays, *Nature* **425**, 817 (2003).
- [10] K. D. Irwin, An application of electrothermal feedback for high resolution cryogenic particle detection, *Applied Physics Letters* **66**, 1998 (1995).
- [11] J. N. Ullom and D. A. Bennett, Review of superconducting transition-edge sensors for x-ray and gamma-ray spectroscopy, *Superconductor Science and Technology* **28**, 084003 (2015).
- [12] I. Charaev, D. A. Bandurin, A. T. Bollinger, I. Y. Phinney, I. Drozdov, M. Colangelo, B. A. Butters, T. Taniguchi, K. Watanabe, X. He, O. Medeiros, I. Božović, P. Jarillo-Herrero, and K. K. Berggren, Single-photon detection using high-temperature superconductors, *Nature Nanotechnology* **18**, 343 (2023).
- [13] L. Cardani, N. Casali, A. Cruciani, H. le Sueur, M. Martinez, F. Bellini, M. Calvo, M. G. Castellano, I. Colantoni, C. Cosmelli, A. D’Addabbo, S. D. Domizio, J. Goupy, L. Minutolo, A. Monfardini, and M. Vignati, Al/ti/al phonon-mediated kIDs for uv–vis light detection over large areas, *Superconductor Science and Technology* **31**, 075002 (2018).
- [14] A. Cruciani, L. Bandiera, M. Calvo, N. Casali, I. Colantoni, G. Del Castello, M. del Gallo Roccagiovine, D. Delicato, M. Giammei, V. Guidi, J. Goupy, V. Pettinacci, G. Pettinari, M. Romagnoni, M. Tamisari, A. Mazzolari, A. Monfardini, and M. Vignati, BULLKID: Monolithic array of particle absorbers sensed by kinetic inductance detectors, *Applied Physics Letters* **121**, 213504 (2022).
- [15] B. A. Mazin, B. Bumble, S. R. Meeker, K. O’Brien, S. McHugh, and E. Langman, A superconducting focal plane array for ultraviolet, optical, and near-infrared astrophysics, *Opt. Express* **20**, 1503 (2012).
- [16] A. Monfardini, A. Benoit, A. Bidaud, L. Swenson, A. Cruciani, P. Camus, C. Hoffmann, F. X. Désert, S. Doyle, P. Ade, P. Maukopf, C. Tucker, M. Roesch, S. Leclercq, K. F. Schuster, A. Endo, A. Baryshev, J. J. A. Baselmans, L. Ferrari, S. J. C. Yates, O. Bourrion, J. Macias-Perez, C. Vescovi, M. Calvo, and C. Giordano, A dual-band millimeter-wave kinetic inductance camera for the iram 30 m telescope, *The Astrophysical Journal Supplement Series* **194**, 24 (2011).
- [17] L. Cardani, N. Casali, G. Catelani, T. Charpentier, M. Clemenza, I. Colantoni, A. Cruciani, L. Gironi, L. Gruenhaupt, D. Gusenkova, *et al.*, Demetra: Suppression of the relaxation induced by radioactivity in superconducting qubits, *Journal of Low Temperature Physics* **199**, 475 (2020).
- [18] M. McEwen, K. C. Miao, J. Atalaya, A. Bilmes, A. Crook, J. Bovaird, J. M. Kreikebaum, N. Zobrist, E. Jeffrey, B. Ying, *et al.*, Resisting high-energy impact events through gap engineering in superconducting qubit arrays, arXiv preprint arXiv:2402.15644 (2024).
- [19] A. P. Vepsäläinen *et al.*, Impact of ionizing radiation on superconducting qubit coherence, *Nature* **584**, 551 (2020).
- [20] M. McEwen *et al.*, Resolving catastrophic error bursts from cosmic rays in large arrays of superconducting qubits, *Nature Physics* **18**, 107 (2021).
- [21] X.-G. Li, J.-H. Wang, Y.-Y. Jiang, G.-M. Xue, X.-X. Cai, J. Zhou, M. Gong, Z.-F. Liu, S.-Y. Zheng, D.-K. Ma, *et al.*, Direct evidence for cosmic-ray-induced correlated errors in superconducting qubit array, arXiv preprint arXiv:2402.04245 (2024).
- [22] C. D. Wilen *et al.*, Correlated charge noise and relaxation errors in superconducting qubits, *Nature* **594**, 369 (2021).
- [23] T. Thorbeck *et al.*, TIs dynamics in a superconducting qubit due to background ionizing radiation (2022), arXiv:2210.04780.
- [24] P. V. Klimov *et al.*, Fluctuations of energy-relaxation times in superconducting qubits, *Phys. Rev. Lett.* **121**, 090502 (2018).
- [25] S. E. de Graaf *et al.*, Direct identification of dilute surface spins on al_2o_3 : Origin of flux noise in quantum circuits, *Phys. Rev. Lett.* **118**, 057703 (2017).
- [26] J. Burnett *et al.*, Evidence for interacting two-level systems from the 1/f noise of a superconducting resonator, *Nature Communications* **5**, 4119 (2014).
- [27] A. Bilmes *et al.*, Resolving the positions of defects in superconducting quantum bits, *Scientific Reports* **10**, 3090 (2020).
- [28] J. Lisenfeld *et al.*, Electric field spectroscopy of material defects in transmon qubits, *npj Quantum Information* **5**, 105 (2019).
- [29] J. M. Martinis *et al.*, Decoherence in josephson qubits from dielectric loss, *Phys. Rev. Lett.* **95**, 210503 (2005).
- [30] C. Müller *et al.*, Towards understanding two-level systems in amorphous solids: insights from quantum circuits, *Reports on Progress in Physics* **82**, 124501 (2019).
- [31] C. R. H. McRae *et al.*, Materials loss measurements using superconducting microwave resonators, *Review of Scientific Instruments* **91**, 091101 (2020).
- [32] G. Bratrud, S. Lewis, K. Anyang, A. Cesani, T. Dyson, H. Magoon, D. Sabhari, G. Spahn, G. Wagner, R. Gualtieri, *et al.*, First measurement of correlated charge noise in superconducting qubits at an underground facility, arXiv preprint arXiv:2405.04642 (2024).
- [33] D. Gusenkova *et al.*, Operating in a deep underground facility improves the locking of gradiometric fluxonium qubits at the sweet spots, *Applied Physics Letters* **120**, 054001 (2022).
- [34] L. Cardani *et al.*, Reducing the impact of radioactivity on quantum circuits in a deep-underground facility, *Nature Communications* **12**, 10.1038/s41467-021-23032-z (2021).
- [35] F. Henriques *et al.*, Phonon traps reduce the quasiparticle density in superconducting circuits, *Applied Physics Letters* **115**, 212601 (2019).
- [36] J. M. Martinis, Saving superconducting quantum processors from decay and correlated errors generated by gamma and cosmic rays, *npj Quantum Information* **7**, 90 (2021).
- [37] V. Iaiya, J. Ku, A. Ballard, C. P. Larson, E. Yelton, C. H. Liu, S. Patel, R. McDermott, and B. L. T. Plourde, Phonon downconversion to suppress correlated errors in superconducting qubits, *Nature Communications* **13**, 6425 (2022).
- [38] P. M. Harrington, M. Li, M. Hays, W. V. D. Pontseele, D. Mayer, H. D. Pinckney, F. Contipelli, M. Gingras,

- B. M. Niedzielski, H. Stickler, J. L. Yoder, M. E. Schwartz, J. A. Grover, K. Serniak, W. D. Oliver, and J. A. Formaggio, Synchronous detection of cosmic rays and correlated errors in superconducting qubit arrays (2024), [arXiv:2402.03208 \[quant-ph\]](#).
- [39] D. T. Le *et al.*, Operating a passive on-chip superconducting circulator: Device control and quasiparticle effects, *Phys. Rev. Research* **3**, 043211 (2021).
- [40] I. J. Arnquist, M. L. di Vacri, N. Rocco, R. Saldanha, T. Schlieder, R. Patel, J. Patil, M. Perez, and H. Uka, Ultra-low radioactivity flexible printed cables, *EPJ Techniques and Instrumentation* **10**, 17 (2023).
- [41] L. Cardani, I. Colantoni, A. Cruciani, F. De Dominicis, G. D’Imperio, M. Laubenstein, A. Mariani, L. Pagnanini, S. Pirro, C. Tomei, N. Casali, F. Ferroni, D. Frolov, L. Gironi, A. Grassellino, M. Junker, C. Kopas, E. Lachman, C. R. H. McRae, J. Mutus, M. Nastasi, D. P. Pappas, R. Pilipenko, M. Sisti, V. Pettinacci, A. Romanenko, D. Van Zanten, M. Vignati, J. D. Withrow, and N. Z. Zhelev, Disentangling the sources of ionizing radiation in superconducting qubits, *The European Physical Journal C* **83**, 94 (2023).
- [42] J. L. Orrell and B. Loer, Sensor-assisted fault mitigation in quantum computation, *Phys. Rev. Applied* **16**, 024025 (2021).
- [43] A. Mariani *et al.*, Mitigation of cosmic rays-induced errors in superconducting quantum processors, IEEE-QCE23 proceedings (2023).
- [44] E. Yelton, C. P. Larson, V. Iaia, K. Dodge, G. L. Magna, P. G. Baity, I. V. Pechenezhskiy, R. McDermott, N. Kurinsky, G. Catelani, and B. L. T. Plourde, Modeling phonon-mediated quasiparticle poisoning in superconducting qubit arrays (2024), [arXiv:2402.15471 \[quant-ph\]](#).
- [45] M. Martinez, L. Cardani, N. Casali, A. Cruciani, G. Pettinari, and M. Vignati, Measurements and simulations of athermal phonon transmission from silicon absorbers to aluminum sensors, *Phys. Rev. Appl.* **11**, 064025 (2019).
- [46] M. Bal, A. A. Murthy, S. Zhu, F. Crisa, X. You, Z. Huang, T. Roy, J. Lee, D. van Zanten, R. Pilipenko, I. Nekrashevich, D. Bafia, Y. Krasnikova, C. J. Kopas, E. O. Lachman, D. Miller, J. Y. Mutus, M. J. Reagor, H. Cansizoglu, J. Marshall, D. P. Pappas, K. Vu, K. Yadavalli, J.-S. Oh, L. Zhou, M. J. Kramer, F. Q. Lecocq, D. P. Goronzy, C. G. Torres-Castaneda, G. Pritchard, V. P. Dravid, J. M. Rondinelli, M. J. Bedzyk, M. C. Hersam, J. Zasadzinski, J. Koch, J. A. Sauls, A. Romanenko, and A. Grassellino, Systematic improvements in transmon qubit coherence enabled by niobium surface encapsulation, *npj Quantum Information* **10**, 43 (2024).
- [47] S. Agostinelli *et al.*, GEANT4—a simulation toolkit, *Nucl. Instrum. Methods. Phys. Res. A* **506**, 250 (2003).
- [48] J. M. Martinis, M. Ansmann, and J. Aumentado, Energy decay in superconducting josephson-junction qubits from nonequilibrium quasiparticle excitations, *Phys. Rev. Lett.* **103**, 097002 (2009).
- [49] M. Lenander, H. Wang, R. C. Bialczak, E. Lucero, M. Mariantoni, M. Neeley, A. D. O’Connell, D. Sank, M. Weides, J. Wenner, T. Yamamoto, Y. Yin, J. Zhao, A. N. Cleland, and J. M. Martinis, Measurement of energy decay in superconducting qubits from nonequilibrium quasiparticles, *Phys. Rev. B* **84**, 024501 (2011).
- [50] L. Stefanazzi, K. Treptow, N. Wilcer, C. Stoughton, S. Montella, C. Bradford, G. Cancelo, S. Saxena, H. Arnaldi, S. Sussman, A. Houck, A. Agrawal, H. Zhang, C. Ding, and D. I. Schuster, The qick (quantum instrumentation control kit): Readout and control for qubits and detectors (2022), [arXiv:2110.00557 \[quant-ph\]](#).
- [51] P. Adari *et al.*, Excess workshop: Descriptions of rising low-energy spectra, *SciPost Physics Proceedings* **10.21468/scipostphysproc.9.001** (2022).
- [52] R. Anthony-Petersen *et al.*, A stress induced source of phonon bursts and quasiparticle poisoning (2022), [arXiv:2208.02790 \[physics.ins-det\]](#).
- [53] G. Angloher *et al.*, Latest observations on the low energy excess in cress-t-iii, *SciPost Physics Proceedings* **10.21468/scipostphysproc.12.013** (2023).
- [54] E. Armengaud *et al.*, Constraints on low-mass wimps from the edelweiss-iii dark matter search, *Journal of Cosmology and Astroparticle Physics* **2016** (05), 019–019.
- [55] R. K. Romani, Aluminium relaxation as the source of excess low energy events in low threshold calorimeters (2024), [arXiv:2406.15425 \[physics.ins-det\]](#).
- [56] S. Kono, J. Pan, M. Chegnizadeh, X. Wang, A. Youssefi, M. Scigliuzzo, and T. J. Kippenberg, Mechanically induced correlated errors on superconducting qubits with relaxation times exceeding 0.4 ms, *Nature Communications* **15**, 3950 (2024).
- [57] V. Verkerke and D. Kirkby, The roofit toolkit for data modeling (2003), [arXiv:0306116](#).

Author Contributions

M.B. and F.C. designed and fabricated the transmon devices. S.Z. performed initial characterization of the qubits. A.C. T.R., F.D.D. and D.H. run the experiments. N.C. developed the Bernoulli algorithm. A.M., F.D.D., T.R. and L.C. performed the data analysis. D.V.Z. helped in writing acquisition software. A.M. performed GEANT4 simulations. I.C., A.P., L.P. and S.P. oversaw the cryostat upgrade for the measurements and the cryogenic operations. T.R., A.M., F.D.D., A.G. and L.C. wrote the manuscript with inputs from all the co-authors in interpreting the results. T.R., A.G. and L.C. conceived and supervised the whole project.

SUPPLEMENT

A. Device Fabrication

The devices are fabricated on a $432\ \mu\text{m}$ thick *c*-plane HEMEX grade double-polished sapphire substrate with 2-inch diameter. The substrate preparation, base-layer (Nb) deposition and Josephson junction evaporation are similar to the fabrication methods followed in Ref. 46. In order to prevent oxidation of the Niobium, a 10 nm thick capping layer is deposited using the same sputtering tool without breaking the vacuum. Gold and Tantalum are used as capping layers for devices Q1 and Q2-Q4 respectively (on two different chips). Device Q1 is first measured at FNAL and then sent to LNGS. The other qubit samples (Q2-Q4) are measured at FNAL. In Table S1, we list the measured parameters of the devices and Fig. S1 shows the relative position of those.

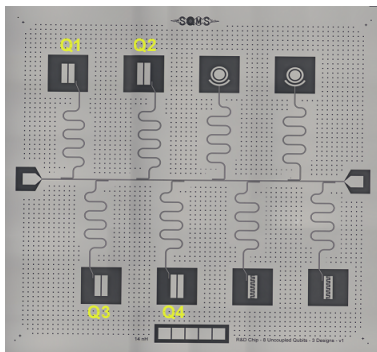


FIG. S1. Chip layout showing relative position of the transmon qubits. The other qubits with concentric and inter-digitated pads are not used in the experiments due to lower T_1 .

B. Measurement Setup

Our measurement setups at the two locations are shown in Fig. S2. The transmon qubit is measured in the hangar geometry, where a $\lambda/4$ CPW readout resonator is coupled to a transmission line. The pulses for both qubit control and readout are sent through a common input line. The input line is attenuated by 60-70 dB distributed between the 4-K and mixing chamber stages. Copper-body 20 dB attenuators are used at the base plate for better thermalization. At LNGS, the input line is also filtered through a 8 GHz reflective low-pass filter and a strong infrared filter (QMC-CRYOIRF-002) to reduce high-frequency noise. The superconducting output line is protected from the incoming noise through a 4-8 GHz triple junctions isolator, an 8 GHz low-pass filter and a weak infrared filter (QMC-CRYOIRF-001). At FNAL, both the input and output lines are filtered through 11 GHz reflective low-pass filters. The superconducting output line also has two 4-8 GHz isolators.

The device boxes at both locations are protected from stray magnetic fields using cryoperm shields. The output signal is first amplified through a commercial HEMT amplifier at the 4-K plate, followed by a room-temperature amplifier outside the fridge before digitization. The qubit control and readout pulses are generated digitally using a RFSoc ZCU 216 evaluation board and the QICK [50] software.

C. Simulation of Interaction Rates

We use the GEANT4-based Monte Carlo simulation developed in Cardani et al. [41] within the SQMS *Round Robin* project with updated parameters. The aim is to predict both the rate of impacts and the amount of energy released in the Sapphire substrate. The geometry implemented in the simulation, shown in Fig. S3, includes (from outside to inside):

- a. An $80 \times 80\ \text{cm}^2$, 5 cm-thick lead base;
- b. An $80 \times 80\ \text{cm}^2$, 5 cm-thick copper base;
- c. 1/2 round of $10 \times 20\ \text{cm}^2$, 5 cm-thick Pb bricks;
- d. 1 round of $10 \times 20\ \text{cm}^2$, 5 cm-thick Pb bricks;
- e. 1 round of $10 \times 66.5\ \text{cm}^2$, 2 cm-thick Cu bars;
- f. A two layers Permimphy magnetic shielding (Outer layer: $55.6\ \text{cm}$ (OD) \times $91.3\ \text{cm}$ (height), 1.5 mm-thick; Inner layer: $51\ \text{cm}$ (ID) \times $89\ \text{cm}$ (height), 1.5 mm-thick);
- g. A $48.1\ \text{cm}$ (OD) \times $119.5\ \text{cm}$ (height) simplified version of the cryostat with internal vessels;
- h. A CryoPerm® magnetic shield below the mixing chamber;
- j. A 3 cm-thick lead plate at 10 mK, placed between the sample and the electronic components used as internal gammas shield;
- k. A $30.23 \times 30.23 \times 6.3\ \text{mm}^3$ gold-plated copper box hosting the chip.

The chip substrate ($7.5 \times 7.5\ \text{mm}^2$, $432\ \mu\text{m}$ -thick HEMEX Sapphire) is considered the only active volume, where we store tracks and record the energy released by each simulated interaction. The main external contributions, namely environmental gammas and muons, are generated according to the methods described in our previous work [41]. For each source, and for both FNAL and INFN-LNGS laboratories, we estimate the rate of interactions in the chip by scaling the number of recorded events to the flux measurements reported in Section 3 of Ref. [41].

Regarding close sources of radioactivity, we simulate the radioactive decays of relevant isotopes (^{40}K , ^{232}Th

Parameter	Q1	Q2	Q3	Q4	Units
Material	Nb/Au	Nb/Ta	Nb/Ta	Nb/Ta	N/A
Qubit frequency	4717.4	4455.4	4451.3	4294.8	MHz
Readout frequency	7206.8	7055.0	6886.5	6714.5	MHz
Qubit π pulse length	0.195	0.091	0.124	0.160	μ s
Readout pulse length	6.0	3.8	4.0	8.0	μ s

TABLE S1. Parameters of devices used in the experiments.

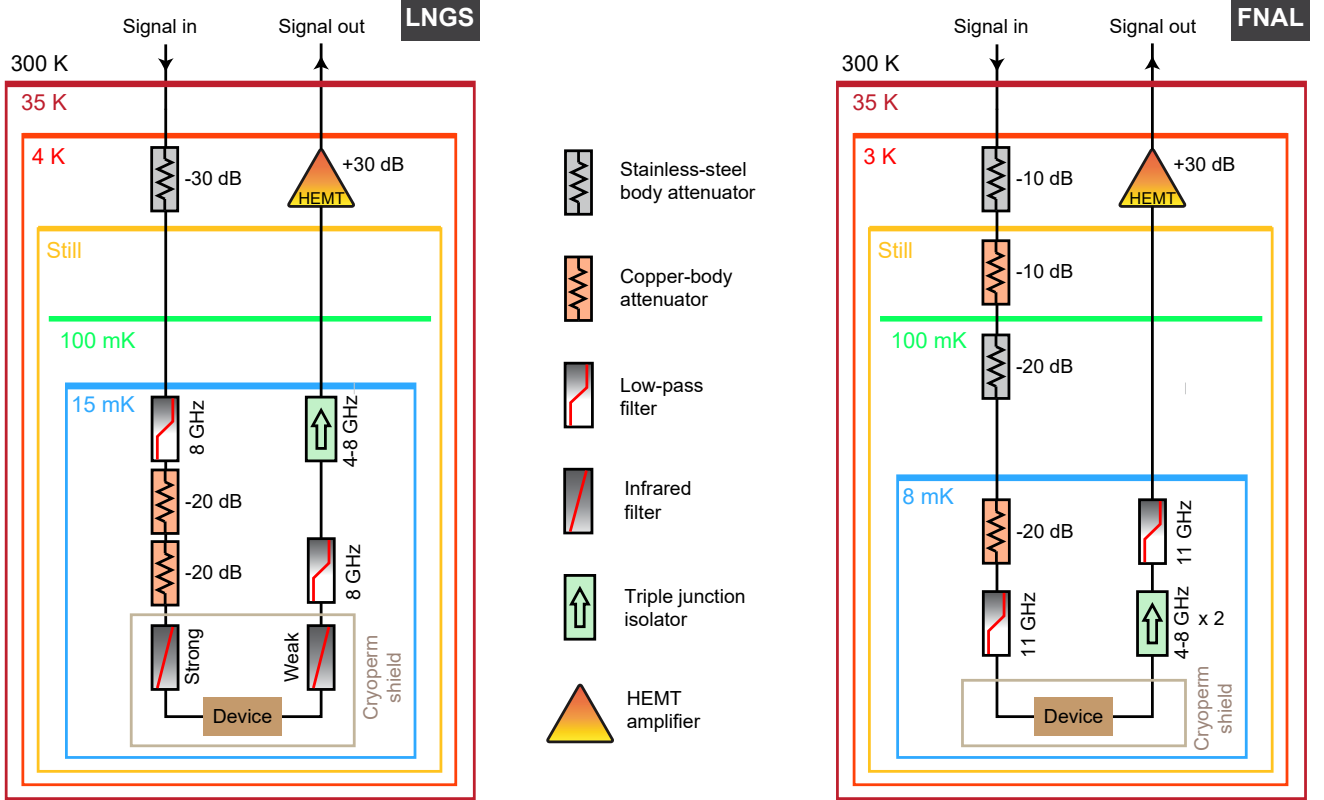


FIG. S2. Cryogenic wiring diagram of the measurement setups at INFN-LNGS and at FNAL.

and ^{238}U chains) uniformly distributed within the volume of the two Printed Circuit Boards (RO4003C produced by ROGERS Corporation) located at the opposite ends of the qubit chip. PCBs indeed constitute the only significant contribution from close sources, as detailed in [41]. We then estimate the rate of interactions in the chip by scaling the number of recorded events to the activities reported in Table S2. These activities are determined by converting the concentrations measured using Inductively Coupled Plasma Mass Spectrometry (ICP-MS) at the Chemistry facility in INFN-LNGS.

Figure S4 presents the results of the Monte Carlo simulation, showing the rate of events as a function of the energy deposited in the qubit substrate for both FNAL and INFN-LNGS facilities. The event rates for each radiation source are reported in Table I. Notably, the overall rate is expected to be approximately an order of mag-

nitude lower at INFN-LNGS (4×10^{-3} event/sec vs. 57×10^{-3} event/sec @FNAL), where the dominant contribution is from the PCBs.

To investigate the rate in the presence of the Thorium radioactive sources used at INFN-LNGS, we generate radioactive decays from a point-like ^{232}Th radioactive source positioned between the external magnetic shield

Source	^{40}K	^{232}Th	^{238}U
	[mBq/kg]	[mBq/kg]	[mBq/kg]
PCB	(518.8 ± 259.4)	(164.0 ± 41.0)	(161.2 ± 49.6)

TABLE S2. Activities of the relevant radioactive isotopes in the RO4003C PCBs produced by ROGERS Corporation. These values were determined by converting the corresponding concentration measured by ICP-MS at the Chemistry facility at INFN-LNGS.

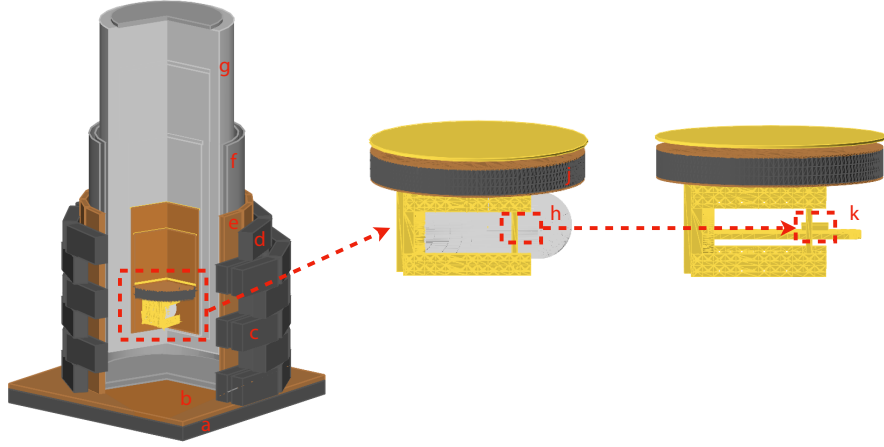


FIG. S3. **Experimental setup of LNGS as implemented in the simulation.** a-e) External gamma shield; f) External two-layer Permimphy magnetic shield; g) Cryostat with internal vessels; h) Internal CryoPerm[®] magnetic shield; j) Internal gamma shield; k) Gold-plated copper box hosting the chip. The full description of the components is reported in the text.

and the copper bars, approximately at the same height of the chip. For this simulation, we consider only gamma emitters in the chain (^{228}Ra , ^{228}Ac , ^{212}Pb , ^{212}Bi and ^{208}Tl), since α and β particles cannot reach the chip as they are shielded by the cryostat. As in the previous case, we determine the rate of interactions in the chip by scaling the number of recorded events to the activities reported in Table S3, which correspond to the Thorium source activities employed in the measurements (and previously characterized using High Purity Germanium spectroscopy). The rate of events in the chip, plotted as a function of the deposited energy for the various

activities, is illustrated in Fig. S3.

Activity [kBq]	Rate [events/sec]
44.2	0.12 ± 0.01
75.9	0.20 ± 0.02
125.4	0.34 ± 0.03
161.0	0.43 ± 0.04

TABLE S3. **Rate of interactions in the Sapphire substrate predicted by the Monte Carlo simulation for different activities of the Thorium sources.** The values used to scale the Monte Carlo simulation correspond to the Thorium source activities employed in the measurements.

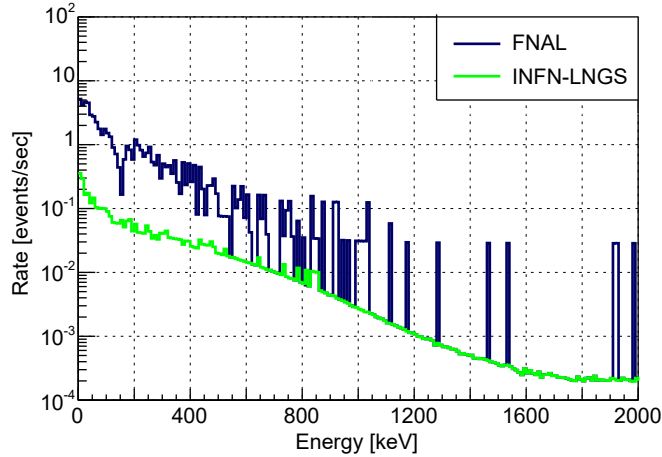


FIG. S4. **Rate of interactions expected in the Sapphire chip as a function of the energy deposited in the chip itself.** The results are shown for both FNAL (blue) and INFN-LNGS (green). In the FNAL case, the total rate is dominated by environmental gammas ($\sim 4.6 \times 10^{-2}$ events/sec), while in the INFN-LNGS scenario the primary contribution comes from radioactive decays in the PCBs ($\sim 2.7 \times 10^{-3}$ events/sec).

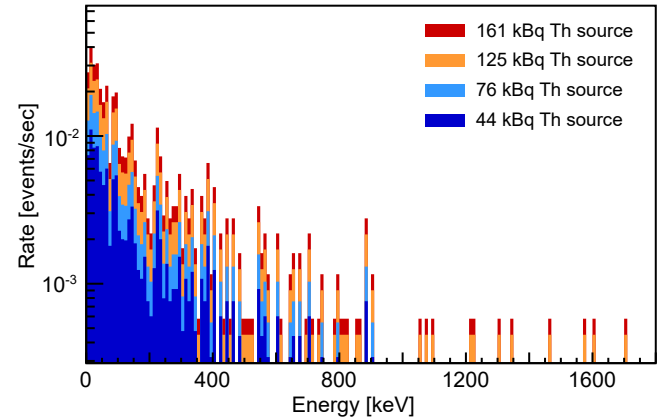


FIG. S5. **Rate of interactions expected in the Sapphire chip as a function of the energy deposited in the chip when exposed to Thorium radioactive sources.** The distinct colors in the plot correspond to the various activities used in the measurements.

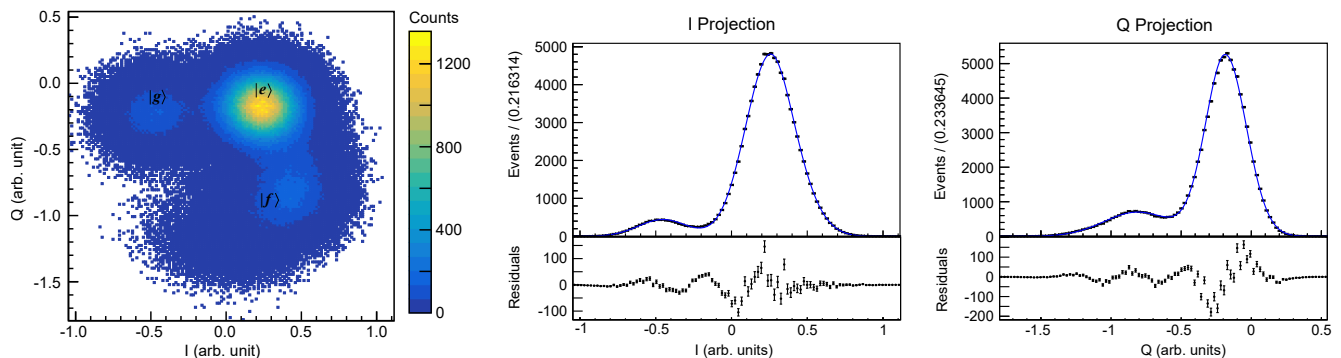


FIG. S6. **Clouds on the I-Q plane corresponding to the qubit states for a subset of the data.** (Left) The clouds corresponding to $|g\rangle$ (left), $|e\rangle$ (upper right), and $|f\rangle$ (bottom right) are visible. (Center and Right) The fits performed on the projected clouds to estimate state populations.

D. Qubit State Discrimination

The I/Q values (in-phase and quadrature-phase signals) obtained from each measurement reflect the state of the qubit. When a large number of measurements are plotted on the I-Q plane, two clusters, corresponding to the states $|g\rangle$ (ground) and $|e\rangle$ (excited), are observed. In our data we observe also signals corresponding to the qubit being in the second excited state $|f\rangle$ and, occasionally, in the third excited state $|h\rangle$. To ensure accuracy we discard measurements where the populations of $|f\rangle$ and $|h\rangle$ are too high.

To identify and exclude periods where the qubit exhibits high populations of the $|f\rangle$ and $|h\rangle$ states, we fit the clouds with 2D Gaussian functions, one for each cluster observed. In our experiment the data are divided into traces of 10^6 measurements. The fit is performed on each trace.

To fit the clouds we use the RooFit toolkit [57]. The fit is performed by projecting the clouds along the two quadratures and simultaneously fitting both projections. The fit function for each projection is given by $\sum_i A_i \cdot f(x, \bar{x}_i, \sigma_i)$, where f is a Gaussian centered in \bar{x}_i and with standard deviation σ_i . Each Gaussian is normalized such that A_i corresponds to the number of measurements associated with that state. The population of a state i is given then by $P_i = A_i / \sum_i A_i$. Fig. S6 shows the clouds produced by a single trace and the result of the simultaneous fit used to estimate state populations.

The clouds corresponding to $|g\rangle$ and $|e\rangle$ are orientated such that their centers are aligned along the same Q value. In this way it is possible to discriminate between the two states by setting a threshold only on the I axis, simplifying state identification.

E. “Effective” T_1 calculation

To calculate the “effective” relaxation time T_1' over a trace of 10^6 points, we perform the following steps:

1. We count the number of times the qubit is in the excited state $|e\rangle$ (N_e) OVER the total number of measurements $N_{\text{tot}} = 10^6$;
2. We calculate T_1' as $-\frac{\Delta t_d}{\log(N_e/N_{\text{tot}})}$.

For each dataset, this process is repeated for each segment of 10^6 points to monitor changes over time, and then we calculate the average $\langle T_1' \rangle$, which is used to estimate the probability of the qubit being in state $|g\rangle$. This method ensures accurate determination of the qubit’s relaxation time by averaging over a large number of measurements.

F. Threshold values

To distinguish events caused by ionizing radiation from those due to qubit spontaneous decay, we employed a consistent analysis approach across all datasets collected at both LNGS and FNAL. Our method involves calculating the probability of observing more than a certain number of zeros within a 60-point signal window using the CDF of the Binomial distribution. This allows us to establish dataset-specific thresholds aimed at minimizing the contribution from qubit spontaneous decay while potentially maximizing sensitivity to radiation-induced events. Specifically, these thresholds are set to target spontaneous qubit decay rates approximately an order of magnitude lower than those expected from ambient radiation sources. Additionally, to mitigate noise-induced triggers, a separate threshold is applied to the pre-trigger region, ensuring robustness in our event selection criteria.

Table S4 summarizes the specific thresholds applied to each dataset, alongside the expected rates from qubit spontaneous decay (calculated using these thresholds), the expected rates from ionizing radiation, and the measured rates.

Datasets	Noise	Signal	Qubit Spontaneous	Ionizing Radiation	Measured
	Threshold	Threshold	Decay Rate	Rate	Rate
	[# of zeros]	[# of zeros]	[events/sec]	[events/sec]	[events/sec]
Shielded chip	15	23	0.0001	0.0040 ± 0.0006	0.003 ± 0.001
44 kBq Th Source	14	24	0.001	0.12 ± 0.01	0.032 ± 0.002
76 kBq Th Source	14	23	0.002	0.20 ± 0.02	0.036 ± 0.004
125 kBq Th Source	15	24	0.004	0.34 ± 0.03	0.052 ± 0.006
161 kBq Th Source	15	24	0.002	0.43 ± 0.04	0.056 ± 0.004
FNAL Q2	10	18	0.002	0.057 ± 0.003	0.003 ± 0.001
FNAL Q3	14	23	0.002	0.057 ± 0.003	0.005 ± 0.001
FNAL Q4	10	18	0.001	0.057 ± 0.003	0.025 ± 0.004

TABLE S4. **Thresholds values, expected rates, and measured rates at LNGS and FNAL.** The table summarizes the specific thresholds applied to each dataset, including the signal thresholds (minimum number of zeros required within the signal window) and noise thresholds (maximum permissible number of zeros in the pre-trigger region). It also presents the expected rates from qubit spontaneous decay, the expected rates from ionizing radiation, and the measured rates. Signal thresholds are set to reduce qubit spontaneous decay events to the rates reported in the third column, while noise thresholds ensure stability in event selection criteria.